Electronic Supplementary Information (ESI) for: Photostability of Oxazoline RNA-precursors in UV-rich Prebiotic Environments

Mikołaj J. Janicki, Samuel J. Roberts, Jiří Šponer, Matthew W. Powner, Robert W. Góra and Rafał Szabla

October 22, 2018

Contents

1 Experimental section

1.1 General Experimental

All compounds were obtained from: *Sigma Aldrich*, *Alfa Aesar* and *Fluorochem* unless specified. UV irradiations were performed using a Rayonet RPR-200 with 6 × RPR-2547A lamps or with 6 × RPR-3000A lamps. Solution pH values were measured with a Corning pH meter 430 with a Fischerbrand FB68801 semi-micro pH probe or a Mettler Toledo Seven Compact pH meter with a Mettler Toledo InLab semi-micro pH probe. Water (H_2O) refers to deionised water produced by an Elga Option 3 purification system unless specified otherwise. Melting points were determined using an *Electrothermal* standard digital apparatus.

Melting points are quoted to the nearest °C and are uncorrected. Bruker NMR spectrometer AVANCE III 600 equipped with a Bruker 5 mm cryoprobe (600 MHz) and Bruker NMR spectrometer AVANCE III 400 with a QNP probe were used to provide ^{1}H NMR data. All spectra were recorded at 298 K. All reported chemical shifts (δ) are given in parts per million (ppm) relative to residual solvent peaks, and ^{1}H spectra calibrated using the residual solvent peaks relative shift to TMS. Coupling constants (J) are given in Hertz (Hz). The following abbreviations refer to spin multiplicities: s (singlet); d (doublet); t (triplet); m (multiplet); or any combination of these. Diastereotopic geminal (AB) spin systems coupled to an additional nucleus are reported as ABX. NMR data are stated as follows: chemical shift (number of protons, multiplicity, coupling constants (J), nuclear assignment). Ultraviolet spectra (UV) were recorded on a Shimadzu UV-1800 UV spectrophotometer. Absorption maxima are reported in wavelength (nm). Infrared spectra (IR) were recorded on a Shimadzu IR Tracer 100 FT-IR spectrometer. Absorption maxima are reported in wavenumber (cm^{-1}).

1.2 Methods

1.2.1 General Irradiation Procedure

A solution of specified thione (6.00 mmol, 2 mM in H_2O/D_2O 9:1) and any other specified species (6.00 mmol, 2 mM in H_2O/D_2O 9:1) was adjusted to pH 6.5 and then degassed with a stream of nitrogen for 3 h in a quartz tube. The tube was sealed with a rubber septum, flushed with argon and then kept under positive pressure argon atmosphere. The solution was irradiated using the specified UV lamps for 16 h at 38°C, then left to relax for 1 h. The solution was lyophilised, and the resulting lyophilite dissolved in D_2O and analysed by NMR spectroscopy. A solution of potassium hydrogen phthalate (0.100 M, 50.0 μL, 5.00 μmol in D_2O) was added as an internal NMR standard and NMR spectra were then reacquired.

1.2.2 Irradiation of arabinose oxazolidinone thione AOT

Arabinose oxazolidinone thione (**AOT**) was submitted to the general irradiation procedure with 254 nm or 300 nm lamps. Analyses of NMR spectra showed that 68% and 83% of **AOT** was returned after irradiation at 254 nm and 300 nm, respectively. After 254 nm irradiation arabinose oxazolidinone (**AOD**) (4%) was observed (Fig. 1).

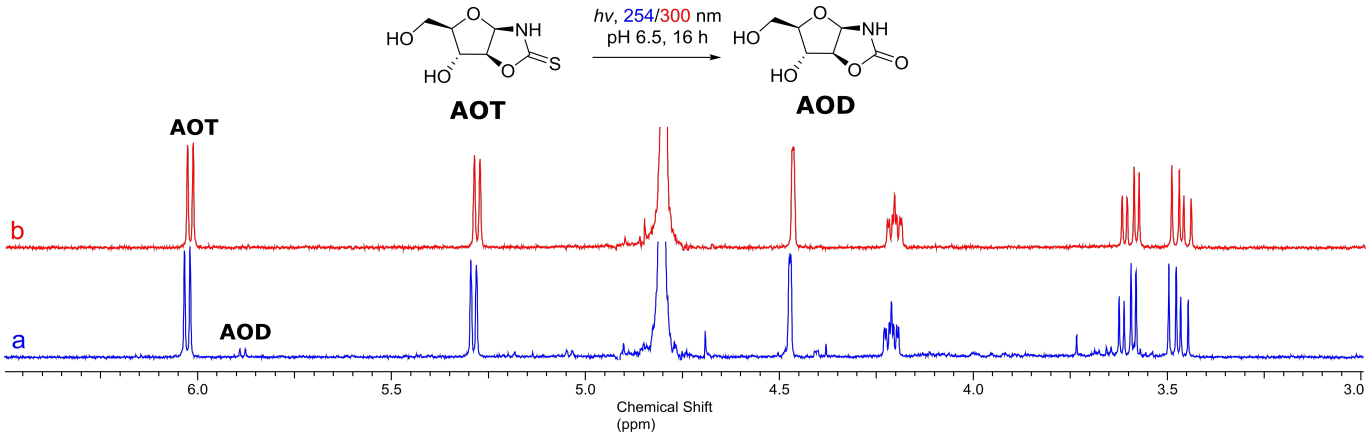

Fig. 1 ^{1}H NMR (600 MHz, D_2O, 3.0–6.5 ppm) spectra show the products of the irradiation of **AOT** (2 mM) in neutral solution. Spectrum (a) show the products of 254 nm irradiation after 16 h. Spectrum (b) to show the products of 300 nm irradiation after 16 h.

1.2.3 Irradiation of ribose oxazolidinone thione ROT

Ribose oxazolidinone thione (**ROT**) was submitted to the general irradiation procedure with 254 nm or 300 nm lamps. Analyses of NMR spectra showed 47% and 78% of **ROT** remained after 254 nm and 300 nm, respectively. After 254 nm irradiation ribose oxazolidinone (**ROD**) (10%) was observed. (Fig. 2).

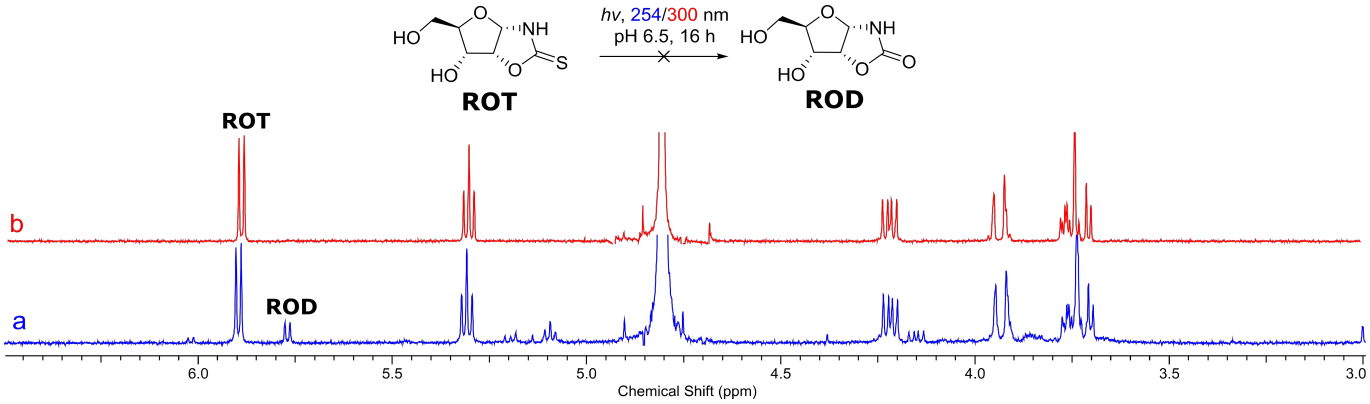

Fig. 2 ^{1}H NMR (600 MHz, D_2O, 3.0–6.5 ppm) spectra show the irradiation of **ROT** (2 mM) in neutral solution. Spectrum (a) show the products of 254 nm irradiation after 16 h. Spectrum (b) show the products of 300 nm irradiation after 16 h

1.2.4 Hydrolysis control of ribose oxazolidinone thione ROT

A solution of **ROT** (0.500 mL, 2.00 mM) at pH 6.5 was heated at 45 °C for 16 h. The solution was cooled and analysed by NMR. Analyses of NMR spectra showed 86% **ROT** remained with no other products visible by NMR (Fig. 3).

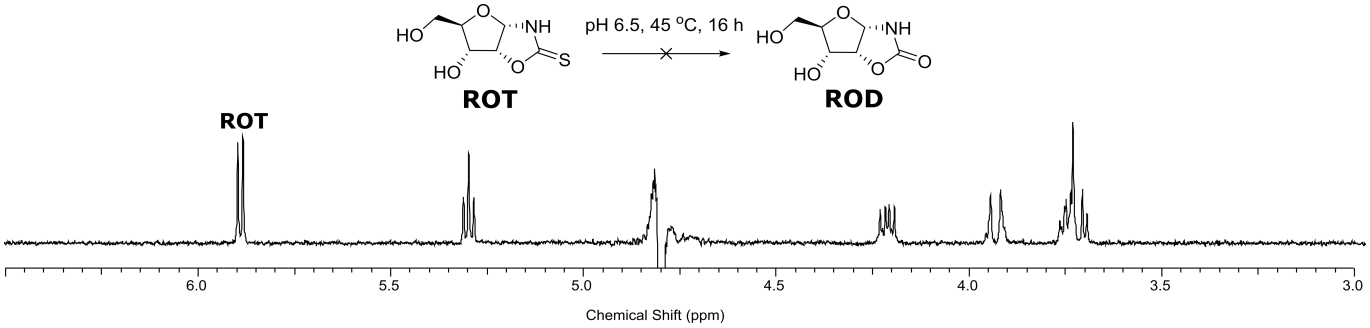

Fig. 3 ^{1}H NMR (600 MHz, D_2O, 3.0–6.5 ppm) spectrum shows the stability of **ROT** (2 mM, pH 6.5) to incubation in H_2O at 45 °C over 16 h.

1.2.5 Simultaneous irradiation of arabinose oxazolidinone thione AOT and adenine A

AOT and adenine (**A**) were submitted to the general irradiation procedure with 254 nm lamps. Analyses of NMR spectra showed that 80% and 100% of **AOT** and adenine were returned, whilst arabinose oxazolidinone (**AOD**) (3%) was observed to form (Fig. 4).

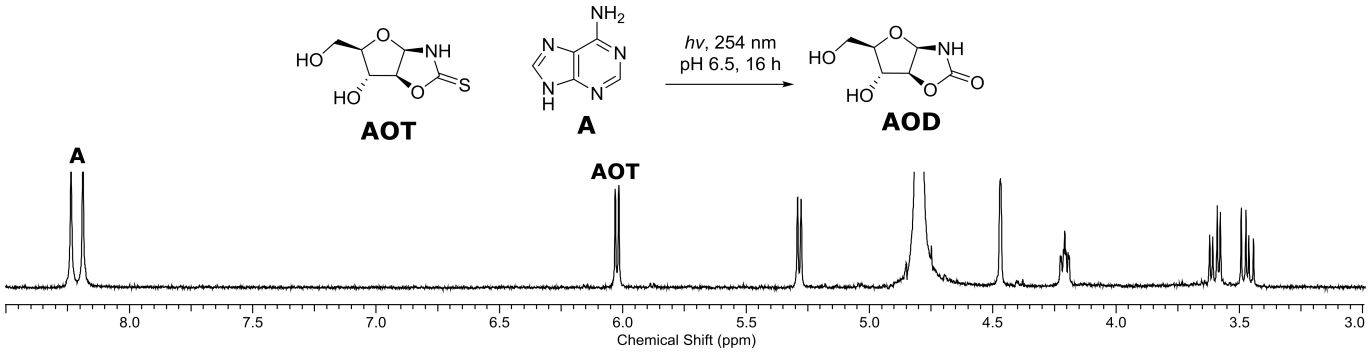

Fig. 4 ^{1}H NMR (600 MHz, D_2O, 3.0–6.5 ppm) spectrum to show the irradiation (254 nm) of **AOT** (2 mM) and adenine (**A**) (2 mM) in neutral solution for 16 h.

1.2.6 Simultaneous irradiation of arabinose oxazolidinone thione AOT and adenosine Adn

AOT and adenosine (**Adn**) were submitted to the general irradiation procedure with 254 nm lamps. Analyses of NMR spectrum showed that 79% and 82% of **AOT** and adenosine (**Adn**) were returned, whilst arabinose oxazolidinone (**AOD**) (9%) was observed to form (Fig. 5).

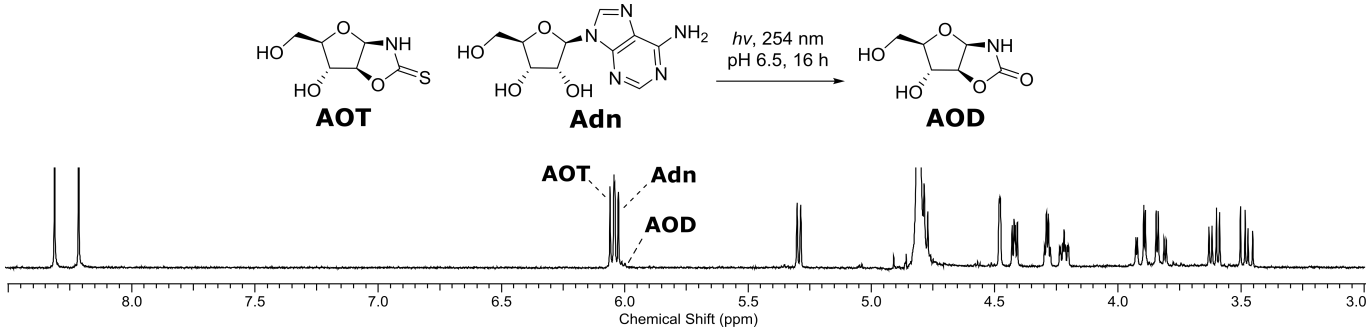

Fig. 5 ^{1}H NMR (600 MHz, D_2O, 3.0–6.5 ppm) spectra to show the irradiation (254 nm) of **AOT** (2 mM) and adenosine (**Adn**) (2 mM) in neutral solution for 16 h.

1.3 Compound Synthesis and Characterisation

1.3.1 Arabinose oxazolidinone thione AOT

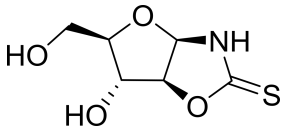

Fig. 6 Arabinose oxazolidinone thione (**AOT**)

Arabinose oxazolidinone thione (**AOT**) compound was synthesised following a literature protocol and the compounds data was found to match the literature values.[1] δ_H (600 MHz, D_2O): 6.07 (1H, d, J = 5.8 Hz, H1′), 5.33 (1H, d, J = 5.8 Hz, H2′), 4.51 (1H, s, H3′), 4.25 (1H, m, H4′), 3.63 (1H, ABX, J = 12.4, 5.3 Hz, H5′), 3.51 (1H, ABX, J = 12.4, 7.5 Hz, H5″); δC (150 MHz, D_2O): 190.0 (C2), 92.5 (H2′), 90.5 (H1′), 87.8 (H4′), 75.2 (H3′), 61.6 (H5′). HRMS (ESI): $C_6H_{10}NO_4S$ predicted mass 192.0331 [M+H], found 192.0332. IR (cm^{-1}): 3394 (NH), 3299 (OH), 2991-2871 (CH), M.P.: seen 137-139 °C. λ_{max} (nm) = 241.

1.3.2 Ribose oxazolidinone thione ROT

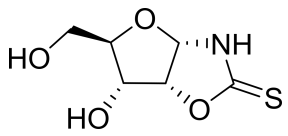

Fig. 7 Ribose oxazolidinone thione (**ROT**)

Ribose oxazolidinone thione (**ROT**) compound was synthesised following a literature protocol and the compounds data was found to match the literature values.[1] δ_H (600 MHz, D_2O): 6.19 (1H, d, J = 5.4 Hz, H1′), 5.36 (1H, t, J = 5.4 Hz, H2′), 4.28 (1H, dd, J = 9.4, 5.4 Hz, H3′), 3.99 (1H, ABX, J = 12.6, 2.0 Hz, H5′), 3.81 (1H, ddd, J = 9.4, 4.8, 2.0 Hz, H4′), 3.77 (1H, ABX, J = 12.6, 4.8 Hz, H5”); δ_C (150 MHz, D_2O): 191.1 (C2), 89.0 (C1′), 85.9 (C2′), 79.3 (C4′), 70.9 (C3′), 60.0 (C5′). HRMS (ESI): $C_6H_{10}NO_4S$ predicted mass 192.0331 [M+H], found 192.0334. IR (cm^{-1}): 3438-3149 (O-H), 2993-2902 (C-H). M.P.: seen 157 °C (decomp). $[\alpha]^{D20}$ +150.2 (c = 0.10, $CHCl_3$). λ_{max} (nm) = 241.

1.4 Compound Spectra

1.4.1 Arabinose oxazolidinone thione AOT

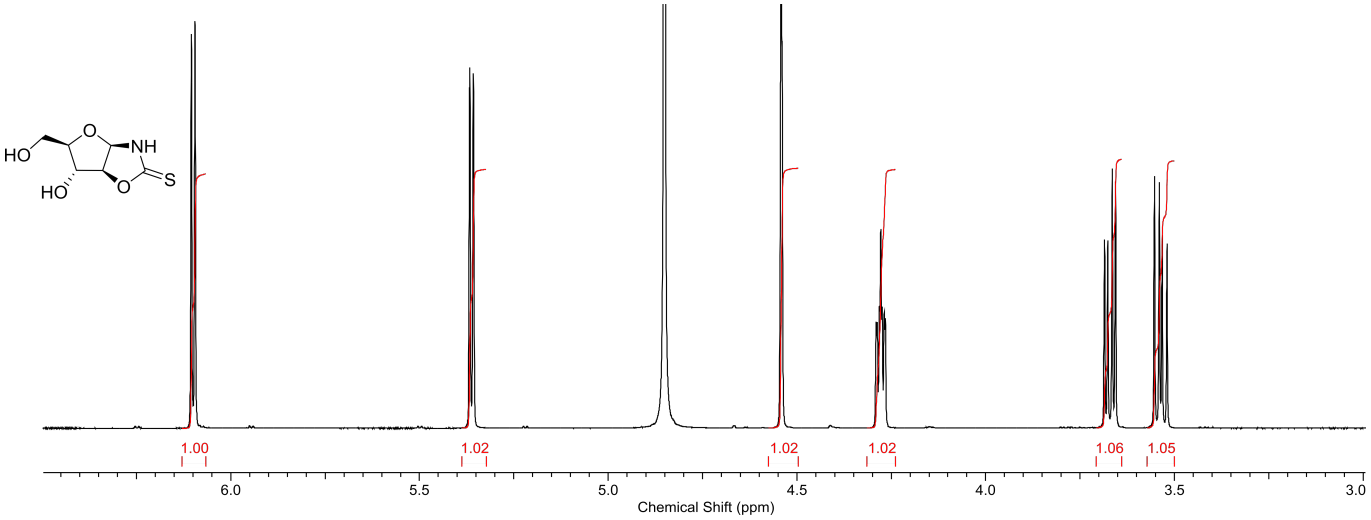

Fig. 8 ^{1}H NMR (600 MHz, D_2O, 3.0–6.5 ppm) spectrum of **AOT**

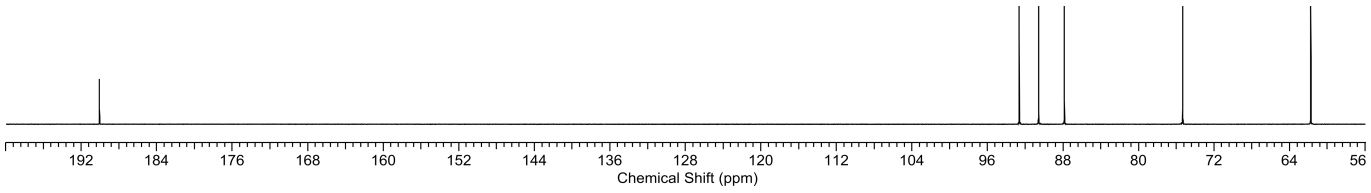

Fig. 9 ^{13}C NMR (150 MHz, DMSO, 56.0–200.0 ppm) spectrum of **AOT**

1.4.2 Ribose oxazolidinone thione ROT

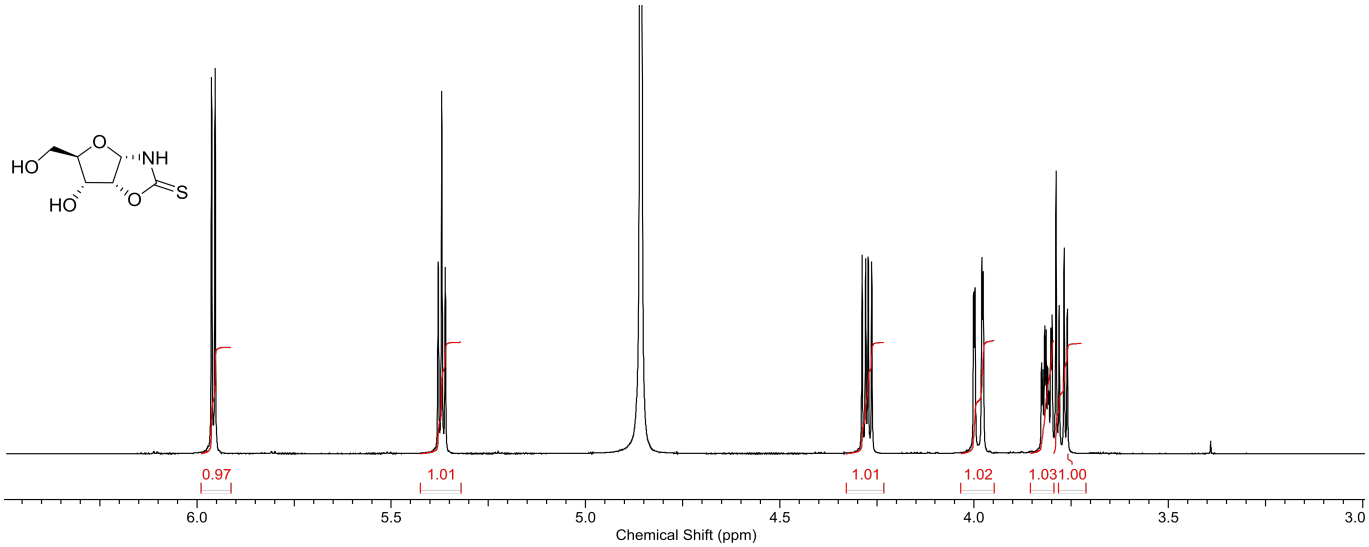

Fig. 10 ^{1}H NMR (600 MHz, D_2O, 3.0–6.5 ppm) spectrum of **ROT**

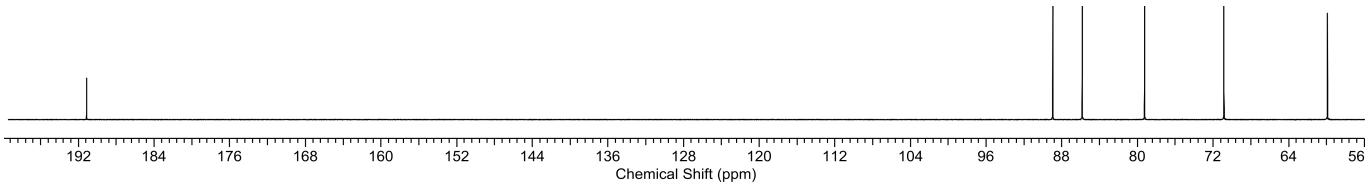

Fig. 11 ^{13}C NMR (150 MHz, DMSO, 56.0–200.0 ppm) spectrum of **ROT**

1.4.3 UV spectra

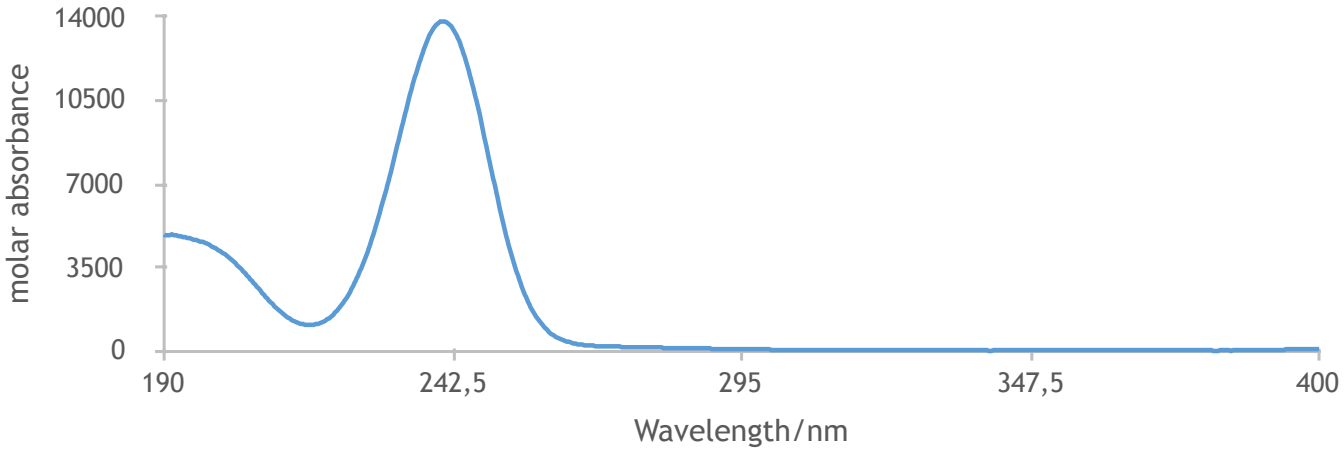

Fig. 12 UV/Vis spectra (400–190 nm, H_2O) of **AOT**

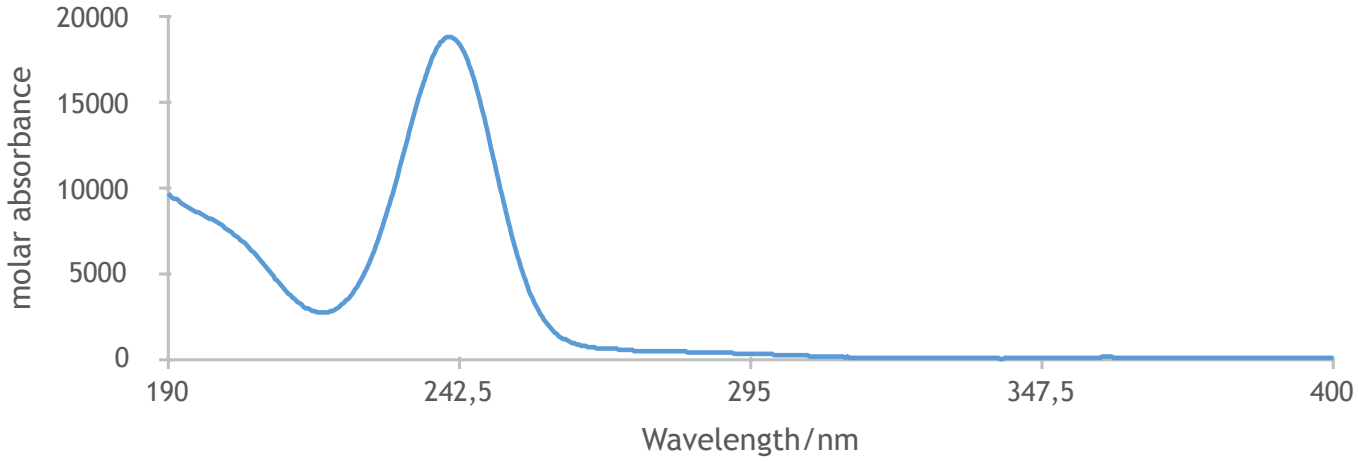

Fig. 13 UV/Vis spectra (400–190 nm, H_2O) of **ROT**

2 Theoretical section

2.1 Computational methods

The ground-state minimum energy structures and harmonic vibrational frequencies were computed using the Kohn–Sham density functional theory (KS-DFT) employing the B3LYP hybrid functional[2], augmented by the D3 dispersion correction[3] with Becke–Johnson damping[4] and the def2-TZVPP basis set.[5] The outlined level of theory is further denoted as B3LYP-D3(BJ)/def2-TZVPP. The implicit solvation model was used to assess relative differences between the Gibbs free energies of pentose oxazolines in order to estimate the most stable arrangements of their sugar ring in bulk water. Solvent effects exerted by bulk water were estimated by performing single-point calculations assuming polarizable continuum model (PCM) for the gas-phase optimized equilibrium geometries located at the B3LYP-D3(BJ)/def2-TZVPP level. The KS-DFT ground state and PCM calculations were performed using Gaussian 16 package.[6]

Stationary points on excited-state potential energy surfaces were located using algebraic diagrammatic construction to the second order method [ADC(2)][7–9] with the cc-pVTZ basis set.[10] Calculations of vertical excitations were performed using the ADC(2)/cc-pVTZ method, assuming the ground-state geometries optimized with the B3LYP-D3(BJ)/def2-TZVPP method. The characters of electronic transitions of the excited states were assigned based on analysis of natural transition orbitals[11] (NTOs) obtained by means of the TheoDore package.[12] Non-equilibrium solvation effects exerted by aquatic environment on the bright excited states were estimated using non-equilibrium polarizable continuum model (PCM) in the perturbed state-specific approach[13,14] with fully perturbative energy- and density-based correction variant, denoted as ptSS-PCM(PTED), combined with the ADC(2)/TZVP method as implemented in the Q-CHEM 5.0 package.[15] The potential energy profiles (PEPs) of plausible radiationless singlet deactivation pathways were obtained by linear interpolation in internal coordinates (LIIC) and the energies of ground and excited electronic states were computed using the MP2 and ADC(2) methods, respectively.[9] The minimum-energy excited state geometries, harmonic vibrational frequencies, vertical excitation energies and PEPs were obtained using the TURBOMOLE 7.1 program.[16]

The minimum-energy crossing points (MECPs) were located utilizing the sequential penalty constrained optimization implemented by Levine et al. in the CIOpt package.[17] These MECPs were optimized using

the energies and analytical gradients obtained at the MP2/ADC(2) level employing the cc-pVTZ basis set. For this purpose we interfaced the CIOpt package[17] with the TURBOMOLE 7.1 program.[16] To validate the geometries in the S_1 minimum and the S_1/S_0 MECPs, these crucial points were reoptimized at the XMS-CASPT2/SA-CASSCF/cc-pVDZ level applying analytical gradients and nonadiabatic couplings implemented in the Bagel program.[18,19] The active space in CASSCF calculations consisted of σ, σ_S, π_S, n_S and π^*, σ_S^*, σ^* orbitals. A similar approach was used to validate the T_1 minimum and $T_1 \rightsquigarrow S_0$ MECP, however, in this case CIOpt package interfaced with the Bagel code was used to optimize these structures utilizing energies and analytical gradients calculated at the XMS-CASPT2/SA-CASSCF/cc-pVDZ level. The active space in calculations for triplet state consisted of σ_S, π_S, n_S and π^*, σ_S^* orbitals. The choice of orbitals in active spaces was based on the rules proposed by Veryazov et al.,[20] who suggested that the natural orbital occupations of active orbitals should be in the range 0.02–1.98.

The spin-orbit couplings (SOCs) were computed for the $S_1 \rightsquigarrow T_2$ MECP (active space: 8 electrons in 7 orbitals) and the $T_1 \rightsquigarrow S_0$ MECP (active space: 8 electrons in 8 orbitals) at the MS-CASPT2/SA-CASSCF/cc-pVTZ-DK level of theory. The scalar relativistic effects were incorporated in the calculations through the 2^{nd} order Douglas–Kroll–Hess Hamiltonian. The intersystem crossing (ISC) rate for the $S_1 \rightarrow T_2$ MECP ISC was estimated applying the time-dependent approach based on the short-time approximation of the time correlation function proposed by Etinski et al.[21] The required vibrational normal modes and harmonic vibrational frequencies for the S_1 and T_2 states were computed at the ADC(2)/cc-pVTZ level. In order to include the mixing of vibrational normal modes after electronic transition, the Duschinsky transformation was employed to represent the final-state normal modes as a linear combination of the initial-state normal modes. The SOCs calculations were conducted using MOLCAS 8.0,[22] ADC(2) calculations were performed in TURBOMOLE 7.1 package,[16] whereas the ISC rate was computed using our in-house code.

The simulated absorption spectra were obtained using the independent mode, displaced harmonic oscillator model (IMDHO).[23,24] The vertical excitation energies, oscillator strengths and excited-state gradients for the 10 and 8 lowest-lying excited states were calculated for O4'-exo **AAO** and C2'-endo **AOT**, respectively, employing the ADC(2)/cc-pVTZ method, assuming the ground-state minimum-energy structures and the ground-state analytical harmonic vibrational frequencies computed at the B3LYP-D3(BJ)/def2-TZVPP level. The absorption spectra were simulated using the ORCA 4.0 program.[25] The ADC(2) and B3LYP-D3 calculations were performed utilizing the TURBOMOLE 7.1 program.[16] Homogeneous line broadenings for electronic transitions required in the IMDHO model were taken as 10 cm^{-1}, whereas the inhomogeneous broadenings were estimated based on QM/MM calculations. In the latter case the molecular dynamics (MD) simulations were used to sample the possible arrangement of water molecules around rigid **AOT** or **AAO**. 500 configurations were then extracted for each system from the final phase of MD simulations. The chosen geometries were further used to calculate vertical excitation energies of **AOT** and **AAO** in the presence of water molecules which were incorporated in quantum mechanical calculations by means of polarizable embedding scheme[26] combined with the CC2/def2-SVP level of theory (PERI-CC2). The estimated inhomogeneous broadenings for electronic bright states of **AOT** and **AAO** amount to 391.2 and 424.2 cm^{-1}, respectively. The technical details of the conducted MD simulations are outlined in the next paragraph.

The ground-state minimum-energy structures of C2'-endo **AOT** and O4'-exo **AAO** obtained at the B3LYP-D3(BJ)/PCM/def2-TZVPP level were assumed in the MD simulations as rigid solutes. The **AOT** and **AAO** molecules were then placed at the center of rectangular boxes composed of either 3384 and 3327 TIP3P[27] water molecules, respectively. The Generalized Amber Force Field (GAFF2) was applied to describe bonding and non-bonding interactions of solutes and their atomic charges were fitted employing CHELPG approach[28] at the B3LYP-D3(BJ)/PCM/def2-TZVPP level with the cutoff distance taken as 12 Å.

In order to obtain reliable sample of configurations from MD simulations we initially optimized rectangular boxes of molecules in 2000 steps. To achieve ambient temperature of systems (300 K), we performed MD simulations within isothermal-isochoric (NVT) ensemble for 1 ns with 0.002 ps time step, using SHAKE scheme to constrain hydrogen atoms. Subsequently, MD simulations based on isothermal-isobaric (NPT) ensemble were conducted for 5 ns to achieve equilibrated systems at ambient conditions (300 K and 1 bar pressure). The final production phase of MD simulations was carried out for 10 ns with the same settings as previously. MD simulations and ab initio calculations were performed using AMBER 16[29] and TURBOMOLE 7.1[16] packages, respectively.

The alternative method of simulating absorption spectra was based on the nuclear ensemble method[30] with 500 points taken from the Wigner distribution for all normal modes computed at the MP2/cc-pVTZ level. Properties of the lowest-lying 10 and 8 excited states, respectively for **AOT** and **AAO**, were calculated using the ADC(2)/cc-pVTZ method to provide excitation energies and oscillator strengths. These absorption spectra were simulated using the NEWTON-X 2.0 package[31,32] interfaced with TURBOMOLE 7.1 program.[16]

2.2 Conformers of arabinose and ribose oxazolidinone thiones and aminooxazolines

Table 1 Vertical excitation energies of **AAO** and **AOT** calculated using the ADC(2)/cc-pVTZ method, assuming the ground-state geometries optimized at the B3LYP-D3(BJ)/def2-TZVPP level. Orbital characters were determined using Natural Transition Orbitals. The values in parentheses were estimated assuming implicit solvent model.

State / Transition		E_{exc}/[eV]	f_{osc}	λ/[nm]
O4'-*exo* arabinose aminooxazoline				
S_1	$\pi\sigma^*$	6.95	0.023	178.4
S_2	$\pi\pi^*$	7.02 (7.08)	0.085	176.6
S_3	$\pi\sigma^*$	7.34	0.005	168.9
S_4	$n_N\pi^*$	7.43	0.103	166.9
C2'-*endo* arabinose oxazolidinone thione				
S_1	$n_S\pi^*$	4.06	0.000	305.4
S_2	$\pi_S\pi^*$	5.32 (5.34)	0.373	233.1
S_3	$n_S\sigma^*$	6.85	0.002	181.0
S_4	$\pi\pi^*$	6.93	0.066	178.9

The Gibbs free energy calculations including water solvent effects at the B3LYP-D3(BJ)/def2-TZVPP/PCM level were performed for the essential conformational arrangements of the sugar ring in arabinose and ribose oxazolidinone thiones (**OT**) and the corresponding aminooxazolines (**AO**) to establish their preferable conformers in bulk water at ambient conditions.

The computational explorations of arabinose **OT** suggest that the C2'-endo (cf. Fig 14) structure is slightly more stable than the C3'-endo conformer (the Gibbs free energy is lower by 1.15 kcal/mol). Consequently, we anticipate that both conformational isomers of **AOT** sugar moiety could be present in water solution. The computed Gibbs free energies of the selected ribose **OT** conformers suggest that the C4'-exo conformer (cf. Fig 14) is more stable by 3.01 kcal/mol than the C2'-endo structure. To verify the effect of substitution of arabinose by ribose in **OT** we computed also the vertical excitation energies for the most

stable C4'-exo **OT** (see Tab. 2 and Tab. 1 in the article). These results show that the vertical excitations of ribose and arabinose **OT** are consistent, even though they were calculated for different sugar rings having different conformations, thus we conclude that different sugar moieties and conformations of **OT** should not result in visible differences in the photophysics and photochemistry of different **OT** forms. This is due to the fact that the orbitals determining the character of the lowest-lying excited states are localized on the oxazoline or oxazolidinone thione fragments.

The computational studies of arabinose **AO** indicate that the O4'-exo conformer should be considered as the most stable arrangement in bulk water (cf. Fig 14), which is lower in Gibbs free energy by merely 1.34 kcal/mol than the C3'-endo structure. Based on these results, we suspect that both the O4'-exo and C3'-endo conformational isomers could be found in aqueous solution. Also in this system the conformational arrangements of the sugar ring should not significantly affect the vertical excitation spectrum. Finally, considering the stability of ribose **AO** conformers, we found only one stable conformational arrangement of the sugar ring which is the C4'-exo structure (cf. Fig 14). The computed vertical excitation energies for this structure, shown in Tab. 2, agree well with the vertical excitation energies computed for the O4'-exo **AAO**.

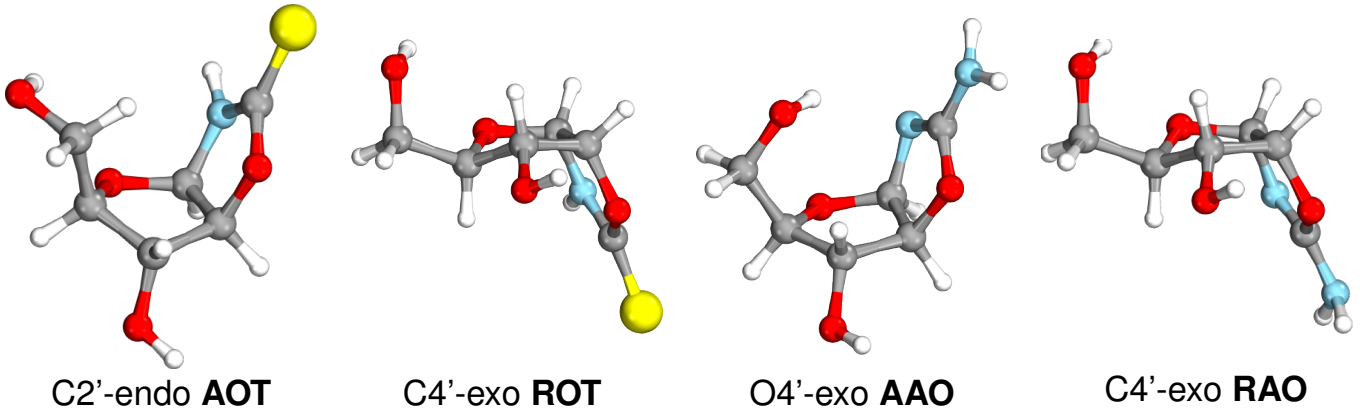

Fig. 14 The ground state structures located at the B3LYP-D3(BJ)/def2-TZVPP level corresponding to the most stable conformational isomers of arabinose and ribose oxazolidinone thiones (**AOT** and **ROT**) and aminooxazolines (**AAO** and **RAO**).

Table 2 Vertical excitation energies of ribose aminooxazoline (**RAO**) and oxazolidinone thione (**ROT**) calculated at the ADC(2)/cc-pVTZ level assuming the equilibrium geometries optimized using the B3LYP-D3(BJ)/def2-TZVPP method. Characters of the excited states were assigned analyzing the natural transition orbitals (NTOs).

State / Transition		E_{exc}/[eV]	f_{osc}	λ/[nm]
C4'-exo **RAO**				
S_1	$\pi\sigma^*$	6.98	0.035	177.6
S_2	$n_N\pi^*$	7.15	0.017	173.4
S_3	$n\sigma^*$	7.26	0.051	170.8
S_4	$\pi\pi^*$	7.29	0.126	170.1
C4'-exo **ROT**				
S_1	$n_S\pi^*$	4.08	0.000	303.9
S_2	$\pi_S\pi^*$	5.34	0.399	232.2
S_3	$n_S\sigma^*$	6.83	0.006	181.5
S_4	$\pi\pi^*$	6.95	0.074	178.4

2.3 A comparison of the simulated UV-absorption spectra

To elucidate the influence of a particular choice of *ab initio* methods and models used to simulate the UV absorption bands of **AOT** and **AAO**, we applied the CC2 and ADC(2) methods combined with the IMDHO and nuclear ensemble frameworks. The resulting simulated spectra along with the available experimental data are shown in Fig. 15. The best agreement with the experimental spectra for **AOT** was obtained applying the IMDHO model (IM) assuming the ground-state minimum energy structure and harmonic vibrational frequencies calculated at the B3LYP-D3(BJ)/def2-TZVPP level and vertical excitation energies and excited-state gradients calculated using the ADC(2)/cc-pVTZ method. The IMDHO spectra simulated at the CC2/cc-pVTZ level are clearly consistent, although the main absorption band for C2'-endo **AOT** is slightly blue-shifted by less than 10 nm.

The alternative (NX) model used for simulating the UV absorption spectra was based on the nuclear ensemble approach using the ADC(2)/cc-pVTZ and MP2/cc-pVTZ methods for excited and ground state calculations, respectively. In the case of C2'-endo **AOT** the NX approach predicted UV absorption spectrum that is consistent with the experimental and the corresponding IM spectrum, although with a smaller broadening.

All simulated UV-absorption spectra of the O4'-exo **AAO** demonstrate very similar features. Interestingly, the electronic ground state of **AAO** computed either at the B3LYP-D3(BJ) or CC2 levels within the IMDHO framework gave virtually identical UV-absorption spectra, and the vertical excitations calculated using the ADC(2) or CC2 methods yielded nearly identical absorption bands peaking around 165 nm. It is worth noting that in this case the NX approach reproduced the coherent picture of UV-spectra, however, with an absorption tail between 190 and 210 nm.

Generally, all tested *ab initio* methods and models used to reproduce vibrational progression show a semi-quantitatively consistent picture of the shape and ranges of absorption bands for **AOT** and **AAO**.

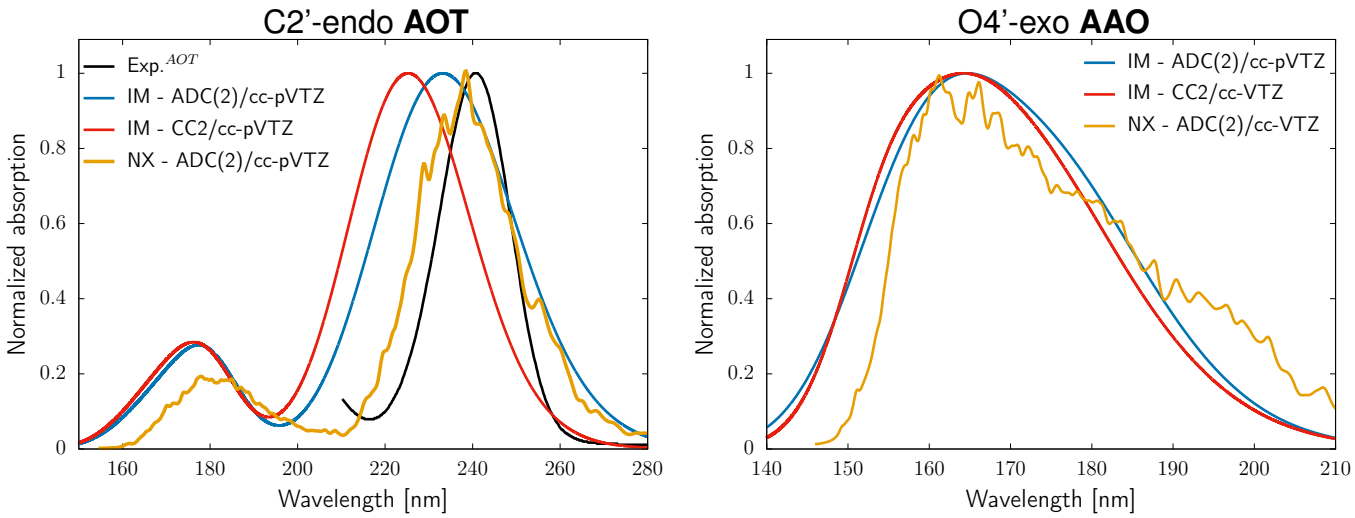

Fig. 15 The UV-absorption spectra of **AOT** and **AAO** simulated using various quantum chemical methods combined with either IMDHO (IM) or nuclear ensemble (NX) models. Blue absorption bands were computed at the ADC(2)/cc-pVTZ level, assuming the S_0 structure optimized at the B3LYP-D3(BJ)/def2-TZVPP level and IM model. The red spectra were obtained applying the CC2/cc-pVTZ method for electronic ground and excited states and IM model. The orange absorption spectra were simulated using the nuclear ensemble model (NX) with ADC(2) and MP2 methods for excited and ground state calculations, respectively, with the cc-pVTZ basis set.

2.4 Solvent effect on the T_1 minimum of AOT

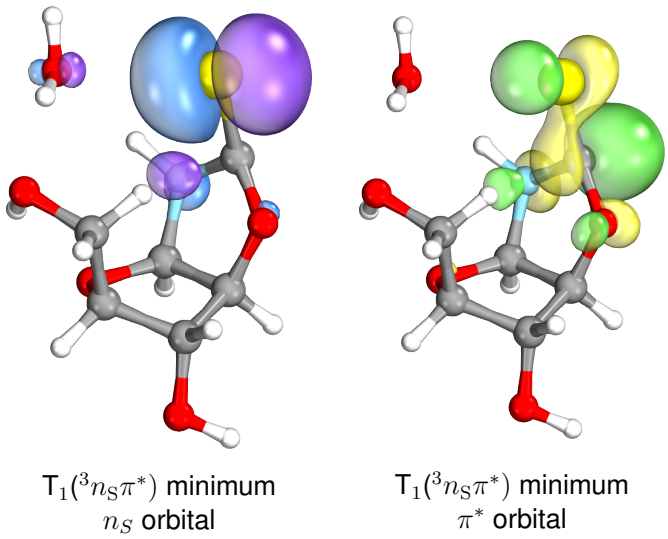

Fig. 16 Minimum-energy geometry of the excited-state complex of **AOT** with one explicit water molecule in the T_1 state, and the associated molecular orbitals.

Recent studies on the photochemistry of microsolvated biomolecules revealed that water might be directly involved in the photorelaxation mechanisms by promoting water-chromophore electron transfer.[33,34] This phenomenon was observed in the case of singlet $n_N\pi^*$ excitations of microhydrated cytosine and adenine.[33,34] To test the direct effect of water on the triplet $^3n_S\pi^*$ state, we included one explicit water molecule in the vicinity of the thiocarbonyl group and performed optimization of the T_1 minimum. The

resulting minimum-energy geometry involved a non-bonding interaction of the $H_2O\cdots S{=}C$ lone electron pairs, analogous to that reported for the water and nitrogen heteroatoms in adenine and cytosine aromatic rings (cf. Fig. 16).[33,34] Formation of the excited-state complex is reflected by an interaction between the p_z orbital of the explicit water molecule and the n_S orbital of the thiocarbonyl group presented in Fig. 16. Interestingly though, this interaction did not result in any considerable charge shift from water to the **AOT** molecule, while the general structural and energetic features of the T_1 minimum of **AOT** clustered with one H_2O remained consistent with the results of the gas phase calculations.

2.5 Excited-state stationary points of AOT

The plausible singlet and triplet photodeactivation channels of the C2'-endo **AOT** were investigated by locating the key stationary points on the excited-state potential energy surfaces at the ADC(2)/cc-pVTZ level. To verify the optimized minimum-energy structures, we employed a multireference electron correlation method XMS-CASTP2 to reoptimize the S_1 and T_1 minima as well as the S_1/S_0 and T_1/S_0 minimum-energy crossing points (MECPs). The ADC(2) (cyan) and XMS-CASPT2 (black) minimum-energy geometries were compared by calculating root-mean-square deviations (RMSDs) of superimposed optimized structures (Fig. 17). The calculated RMSDs show that the ADC(2) structures are virtually identical with the XMS-CASPT2 geometries. Considering the the relative energy differences between the S_1 minimum-energy structure and the S_1/S_0 MECP calculated either at the ADC(2) and XMS-CASPT2 levels, these are also nearly identical and amount to 0.26 and 0.28 eV, respectively. On the other hand, the energy difference between the T_1 minimum-energy structure and the T_0/S_0 MECP calculated using the ADC(2) and XMS-CASPT2 methods equal to 0.18 and 0.22 eV, respectively. These results demonstrate that the radiationless deactivation channels predicted at the ADC(2) level should be reliable.

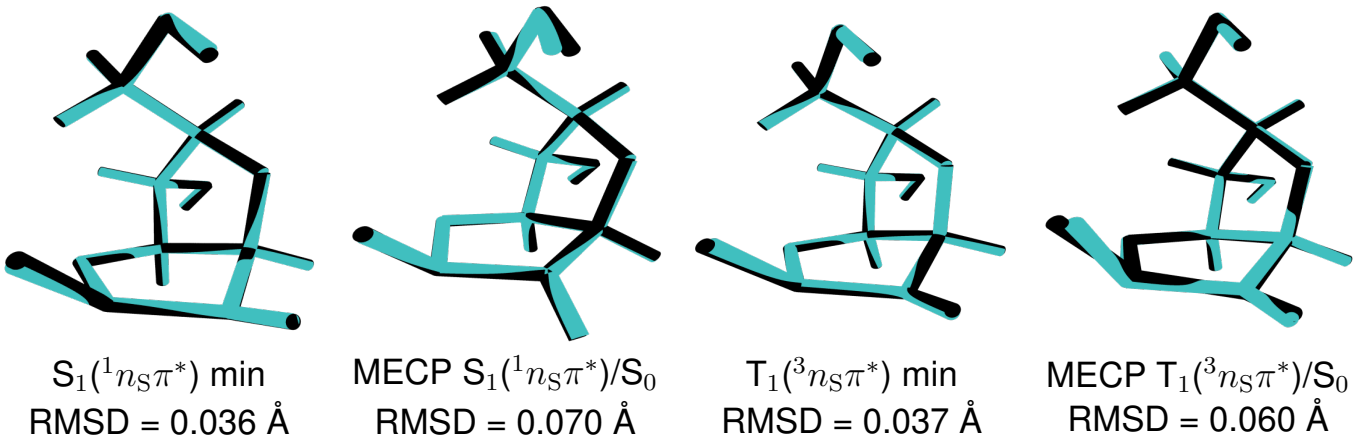

Fig. 17 The superimposed minimum-energy structures optimized at the either ADC(2)/cc-pVTZ (cyan) or XMS-CASPT2/SA-CASSCF/cc-pVDZ levels (black).

References

1 S. Stairs, A. Nikmal, D.-K. Bučar, S.-L. Zheng, J. W. Szostak and M. W. Powner, *Nat. Commun.*, 2017, **8**, 15270.

2 A. D. Becke, *J. Chem. Phys.*, 1993, **98**, 5648–5652.

3 S. Grimme, J. Antony, S. Ehrlich and H. Krieg, *J. Chem. Phys.*, 2010, **132**, 154104.

4 S. Grimme, S. Ehrlich and L. Goerigk, *J. Comput. Chem.*, 2011, **32**, 1456–1465.
5 F. Weigend and R. Ahlrichs, *Phys. Chem. Chem. Phys.*, 2005, **7**, 3297–3305.
6 M. J. Frisch, G. W. Trucks, H. B. Schlegel, G. E. Scuseria, M. A. Robb, J. R. Cheeseman, G. Scalmani, V. Barone, G. A. Petersson, H. Nakatsuji, X. Li, M. Caricato, A. V. Marenich, J. Bloino, B. G. Janesko, R. Gomperts, B. Mennucci, H. P. Hratchian, J. V. Ortiz, A. F. Izmaylov, J. L. Sonnenberg, D. Williams-Young, F. Ding, F. Lipparini, F. Egidi, J. Goings, B. Peng, A. Petrone, T. Henderson, D. Ranasinghe, V. G. Zakrzewski, J. Gao, N. Rega, G. Zheng, W. Liang, M. Hada, M. Ehara, K. Toyota, R. Fukuda, J. Hasegawa, M. Ishida, T. Nakajima, Y. Honda, O. Kitao, H. Nakai, T. Vreven, K. Throssell, J. A. Montgomery, Jr., J. E. Peralta, F. Ogliaro, M. J. Bearpark, J. J. Heyd, E. N. Brothers, K. N. Kudin, V. N. Staroverov, T. A. Keith, R. Kobayashi, J. Normand, K. Raghavachari, A. P. Rendell, J. C. Burant, S. S. Iyengar, J. Tomasi, M. Cossi, J. M. Millam, M. Klene, C. Adamo, R. Cammi, J. W. Ochterski, R. L. Martin, K. Morokuma, O. Farkas, J. B. Foresman and D. J. Fox, *Gaussian˜16 Revision A.03*, 2016, Gaussian Inc. Wallingford CT.
7 J. Schirmer, *Phys. Rev. A*, 1982, **26**, 2395–2416.
8 A. Dreuw and M. Wormit, *Wiley Interdiscip. Rev. Comput. Mol. Sci.*, **5**, 82–95.
9 C. Hättig, *Adv. Quantum Chem.*, 2005, **50**, 37–60.
10 T. H. Dunning, *J. Chem. Phys.*, 1989, **90**, 1007–1023.
11 R. L. Martin, *J. Chem. Phys.*, 2003, **118**, 4775–4777.
12 *F. Plasser, "TheoDORE 1.4: A package for theoretical density, orbital relaxation, and exciton analysis"*. `http://theodore-qc.sourceforge.net (2018).`
13 J.-M. Mewes, Z.-Q. You, M. Wormit, T. Kriesche, J. M. Herbert and A. Dreuw, *J. Phys. Chem. A*, 2015, **119**, 5446–5464.
14 J.-M. Mewes, J. M. Herbert and A. Dreuw, *Phys. Chem. Chem. Phys.*, 2017, **19**, 1644–1654.
15 Y. Shao, Z. Gan, E. Epifanovsky, A. T. B. Gilbert, M. Wormit, J. Kussmann, A. W. Lange, A. Behn, J. Deng, X. Feng, D. Ghosh, M. Goldey, P. R. Horn, L. D. Jacobson, I. Kaliman, R. Z. Khaliullin, T. Kuś, A. Landau, J. Liu, E. I. Proynov, Y. M. Rhee, R. M. Richard, M. A. Rohrdanz, R. P. Steele, E. J. Sundstrom, H. L. W. III, P. M. Zimmerman, D. Zuev, B. Albrecht, E. Alguire, B. Austin, G. J. O. Beran, Y. A. Bernard, E. Berquist, K. Brandhorst, K. B. Bravaya, S. T. Brown, D. Casanova, C.-M. Chang, Y. Chen, S. H. Chien, K. D. Closser, D. L. Crittenden, M. Diedenhofen, R. A. D. Jr, H. Do, A. D. Dutoi, R. G. Edgar, S. Fatehi, L. Fusti-Molnar, A. Ghysels, A. Golubeva-Zadorozhnaya, J. Gomes, M. W. D. Hanson-Heine, P. H. P. Harbach, A. W. Hauser, E. G. Hohenstein, Z. C. Holden, T.-C. Jagau, H. Ji, B. Kaduk, K. Khistyaev, J. Kim, J. Kim, R. A. King, P. Klunzinger, D. Kosenkov, T. Kowalczyk, C. M. Krauter, K. U. Lao, A. D. Laurent, K. V. Lawler, S. V. Levchenko, C. Y. Lin, F. Liu, E. Livshits, R. C. Lochan, A. Luenser, P. Manohar, S. F. Manzer, S.-P. Mao, N. Mardirossian, A. V. Marenich, S. A. Maurer, N. J. Mayhall, E. Neuscamman, C. M. Oana, R. Olivares-Amaya, D. P. O'Neill, J. A. Parkhill, T. M. Perrine, R. Peverati, A. Prociuk, D. R. Rehn, E. Rosta, N. J. Russ, S. M. Sharada, S. Sharma, D. W. Small, A. Sodt, T. Stein, D. Stück, Y.-C. Su, A. J. W. Thom, T. Tsuchimochi, V. Vanovschi, L. Vogt, O. Vydrov, T. Wang, M. A. Watson, J. Wenzel, A. White, C. F. Williams, J. Yang, S. Yeganeh, S. R. Yost, Z.-Q. You, I. Y. Zhang, X. Zhang, Y. Zhao, B. R. Brooks, G. K. L. Chan, D. M. Chipman, C. J. Cramer, W. A. G. III, M. S. Gordon, W. J. Hehre, A. Klamt, H. F. S. III, M. W. Schmidt, C. D. Sherrill, D. G. Truhlar, A. Warshel, X. Xu, A. Aspuru-Guzik, R. Baer, A. T. Bell, N. A. Besley, J.-D. Chai, A. Dreuw, B. D. Dunietz, T. R. Furlani, S. R. Gwaltney, C.-P. Hsu, Y. Jung, J. Kong, D. S. Lambrecht, W. Liang, C. Ochsenfeld, V. A. Rassolov, L. V. Slipchenko, J. E. Subotnik, T. V. Voorhis, J. M. Herbert, A. I. Krylov, P. M. W. Gill and M. Head-Gordon, *Mol. Phys.*, 2015, **113**, 184–215.

16 *TURBOMOLE V7.1 2016, a development of University of Karlsruhe and Forschungszentrum Karlsruhe GmbH, 1989-2007, TURBOMOLE GmbH, since 2007; available from* `http://www.turbomole.com`.
17 B. G. Levine, J. D. Coe and T. J. Martínez, *J. Phys. Chem. B*, 2008, **112**, 405–413.
18 *BAGEL, Brilliantly Advanced General Electronic-structure Library.* `http://www.nubakery.org` `under the GNU General Public License`.
19 T. Shiozaki, *Wiley Interdiscip. Rev. Comput. Mol. Sci.*, 2018, **8**, e1331.
20 V. Veryazov, P. Å. Malmqvist and B. O. Roos, *Int. J. Quantum Chem.*, 2011, **111**, 3329–3338.
21 M. Etinski, J. Tatchen and C. M. Marian, *J. Chem. Phys.*, 2011, **134**, 154105.
22 F. Aquilante, J. Autschbach, R. K. Carlson, L. F. Chibotaru, M. G. Delcey, L. De Vico, I. Fdez. Galván, N. Ferré, L. M. Frutos, L. Gagliardi, M. Garavelli, A. Giussani, C. E. Hoyer, G. Li Manni, H. Lischka, D. Ma, P. Malmqvist, T. Müller, A. Nenov, M. Olivucci, T. B. Pedersen, D. Peng, F. Plasser, B. Pritchard, M. Reiher, I. Rivalta, I. Schapiro, J. Segarra-Martí, M. Stenrup, D. G. Truhlar, L. Ungur, A. Valentini, S. Vancoillie, V. Veryazov, V. P. Vysotskiy, O. Weingart, F. Zapata and R. Lindh, *J. Comput. Chem.*, 2016, **37**, 506–541.
23 T. Petrenko and F. Neese, *J. Chem. Phys.*, 2007, **127**, 164319.
24 T. Petrenko and F. Neese, *J. Chem. Phys.*, 2012, **137**, 234107.
25 F. Neese, *Wiley Interdiscip. Rev. Comput. Mol. Sci.*, 2012, **2**, 73–78.
26 T. Schwabe, K. Sneskov, J. M. Haugaard Olsen, J. Kongsted, O. Christiansen and C. Hättig, *J. Chem. Theory Comput.*, 2012, **8**, 3274–3283.
27 W. L. Jorgensen, J. Chandrasekhar, J. D. Madura, R. W. Impey and M. L. Klein, *J. Chem. Phys.*, 1983, **79**, 926–935.
28 C. M. Breneman and K. B. Wiberg, *J. Comput. Chem.*, **11**, 361–373.
29 D. Case, R. Betz, D. Cerutti, T. Cheatham, T. Darden, R. Duke, T. Giese, H. Gohlke, A. Goetz, N. Homeyer, S. Izadi, P. Janowski, J. Kaus, A. Kovalenko, T. Lee, S. LeGrand, P. Li, C. Lin, T. Luchko, B. Madej, R. Luo, D. Mermelstein, K. Merz, G. Monard, H. Nguyen, H. Nguyen, I. Omelyan, A. Onufriev, D. Roe, A. Roitberg, C. Sagui, C. Simmerling, W. Botello-Smith, J. Swails, R. Walker, J. Wang, R. Wolf, X. Wu, L. Xiao and P. Kollman, *AMBER 2016, University of California and San Francisco*.
30 R. Crespo-Otero and M. Barbatti, *Theor. Chem. Acc.*, 2012, **131**, 1–14.
31 M. Barbatti, M. Ruckenbauer, F. Plasser, J. Pittner, G. Granucci, M. Persico and H. Lischka, *Wiley Interdiscip. Rev. Comput. Mol. Sci.*, 2014, **4**, 26–33.
32 *Barbatti, M.; Granucci, G.; Ruckenbauer, M.; Plasser, F.; Crespo-Otero, R.; Pittner, J.; Persico, M.; Lischka, H., "NEWTON-X: A package for Newtonian dynamics close to the crossing seam. Version 2, 2016",* `www.newtonx.org`.
33 M. Barbatti, *J. Am. Chem. Soc.*, 2014, **136**, 10246–10249.
34 R. Szabla, H. Kruse, J. Šponer and R. W. Góra, *Phys. Chem. Chem. Phys.*, 2017, **19**, 17531–17537.